Helmholtz-Zentrum Dresden-Rossendorf (HZDR)

HELMHOLTZ ZENTRUM
DRESDEN ROSSENDORF

Second harmonic generation from precise diamond blade diced ridge waveguides

Xu, H.; Li, Z.; Pang, C.; Li, R.; Li, G.; Akhmadaliev, S.; Zhou, S.; Lu, Q.; Jia, Y.; Chen, F.;

Originally published:

February 2022

Chinese Physics B 31(2022), 094209

DOI: https://doi.org/10.1088/1674-1056/ac5242

Perma-Link to Publication Repository of HZDR:

https://www.hzdr.de/publications/Publ-34807

Release of the secondary publication
on the basis of the German Copyright Law § 38 Section 4.

Cover sheet 30.10.2026 16:51:17

Second harmonic generation from precise diamond blade diced ridge waveguides*

Hui Xu(徐慧)[1], Ziqi Li(李子琦)[1,2], Chi Pang(逄驰)[1], Rang Li(李让)[1,3], Genglin Li(李庚霖)[1], Sh. Akhmadaliev[3], Shengqiang Zhou(周生强)[3], Qingming Lu(路庆明)[4], Yuechen Jia(贾曰辰)[1,†], and Feng Chen(陈峰)[1]

[1]*School of Physics, State Key Laboratory of Crystal Materials, Shandong University, Jinan, 250100, China*

[2]*Division of Physics and Applied Physics, School of Physical and Mathematical Sciences, Nanyang Technological University, Singapore 637371, Singapore*

[3]*Institute of Ion Beam and Materials Research, Helmholtz-Zentrum Dresden-Rossendorf, Dresden 01314, Germany*

[4]*School of Chemistry and Chemical Engineering, Shandong University, Jinan, 250100, China*

In this work, carbon ion irradiation and precise diamond blade dicing are applied for Nd:GdCOB ridge waveguide fabrication. The propagation properties of the fabricated Nd:GdCOB waveguides are investigated through experiments and theoretical analysis. The micro-Raman analysis reveals that the lattice of Nd:GdCOB crystal expands during the irradiation process. The micro-second harmonic spectroscopic analysis suggests that the original nonlinear properties of the Nd:GdCOB crystal are greatly enhanced within the waveguide volume. Under a pulsed 1064-nm laser pumping, second harmonic generation (SHG) at 532 nm have been achieved in the fabricated waveguides. The maximum SHG conversion efficiencies are determined to be ~8.32%W^{-1} and ~22.36%W^{-1} for planar and ridge waveguides, respectively.

* Project supported by "Taishan Scholars Youth Expert Program" of Shandong Province, "Qilu Young Scholar Program" of Shandong University, China.

† Corresponding author. E-mail: yuechen.jia@sdu.edu.cn

Accepted Manuscript

Keywords: Optical waveguides, Nd:GdCOB crystal, Second harmonic generation

PACS: 42.79.Gn, 42.70.Mp, 42.65.-k

Introduction

Optical waveguide, as one of the essential components of integrated photonics, can confine light fields in extremely small volumes [1,2]. As a result, the light intensity obtained from the waveguide volume is much higher than that in bulks [3,4]. This feature provides meaningful advantages in nonlinear optical applications, where various nonlinear phenomena could be generated from the waveguide structure at a relatively low optical power. For example, frequency conversion processes based on waveguides feature higher conversion efficiencies and more flexible mode selections in comparison with those based on the bulks [4]. Combining the versatility of multifunctional crystals with the compact geometries of waveguide structures, crystalline waveguides can be used for construction of multifunctional optical devices with small footprints, such as on-chip lasers, compact optical modulators and nonlinear wavelength converters [5-7]. In practice, channel or ridge waveguides with light field confinement in two dimensions (2D) are preferred than one-dimensional (1D) planar waveguides due to their better optical confinement and more flexible geometries [8].

Ion implantation, as an important material modification method, has been applied to a variety of crystals [9-15]. By bombarding the target crystal surface with energetic ion beams, localized lattice damages and refractive index modifications at near-surface regions appear, resulting in optical waveguide formation [16-18]. Up to now, this technique has been applied to waveguide preparation in dozens of crystalline materials [3,16]. Optical waveguides manufactured by ion implantation are generally in 1D planar structures. Additional surface microfabrication is therefore needed to obtain 2D waveguide structures. Of the techniques used for surface microfabrication, femtosecond-laser-direct writing (FsLDW) and precise diamond blade dicing are the most commonly-used ones. Both techniques have been utilized to manufacture ridge waveguides based on ion-irradiated Nd:YAG planar waveguide

Accepted Manuscript

[19-23]. However, compared with the ridge waveguides fabricated by FsLDW, those prepared by precise diamond blade dicing feature lower scattering losses and higher optical quality owing to their smoother side walls [19,24-26].

Combining the lasing and luminescence characteristics of Nd^{3+} ions with the nonlinear optical properties of GdCOB matrix, it is shown that neodymium-doped $GdCa_4O(BO_3)_3$ (Nd:GdCOB) has attractive optical properties as an excellent laser gain medium and an efficient self-frequency doubling (SFD) crystal [27-31]. In previous works, planar and channel waveguides have been fabricated in Nd:GdCOB crystals by ion irradiation [32] and FsLDW [33], and second harmonic generation (SHG) have also been achieved using these waveguide structures. However, up to now, Nd:GdCOB ridge waveguides produced by ion irradiation and precise diamond dicing has not been reported.

In this work, we demonstrate the fabrication of Nd:GdCOB ridge waveguides by combining ion beam irradiation with precise diamond blade dicing techniques. We performed SHG at 532 nm in both ridge and planar waveguides using 1064-nm pulsed fundamental wave.

2. Experiments

The 8 at.% Nd-doped GdCOB crystal used in this work was cut to satisfy Type-Ⅰ phase matching condition (θ= 161.5°, ϕ = 0°) with the dimension of 11×9×2.2 mm^3. The crystal facets of 11×9 mm^2 and 11×2.2 mm^2 were well polished to an optical grade. As Fig. 1(a) shows, the surface of the sample was irradiated by carbon (C^{5+}) ions with an energy of 15 MeV at a fluence of 2×10^{14} ions/cm^2. As a result, a planar waveguide with a thickness of ~10 μm (according to the microscopic image and the ion irradiation calculations, as presented in the following section) is achieved. The ion irradiation was accomplished by the 3MV tandem accelerator at Helmholtz-Zentrum Dresden-Rossendorf, Germany. To reduce channel effect, the incident ion beam was deviated by 7° from the normal of the sample surface. After that, based on the planar configuration, we constructed ridge waveguides using diamond blade dicing (see Fig. 1(b)). During this process, several air grooves perpendicular to the crystal surface with a size of approximately 11×2.2 mm^2 were produced with the blade (DISCO Corp., P1A851 SD3000R10B10 [34]) installed on a precision dicing machine

Accepted Manuscript

(Jingchuang Advanced, AR3000). The rotation and movement velocities were set to 20,000 r/min and 0.05 mm/s, respectively. With the vertical optical confinement provided by ion induced refractive index change and the lateral optical confinement offered by two neighboring grooves, ridge waveguides with widths of 10 μm (WG1), 20 μm (WG2), 25 μm (WG3), and 30 μm (WG4) formed. Both ion irradiation and precise diamond blade dicing are high-precision waveguide fabrication methods with good reproducibility and robustness[35-37], and the fabrication errors have negligible impacts on the waveguide properties according to simulation results.

Fig. 1

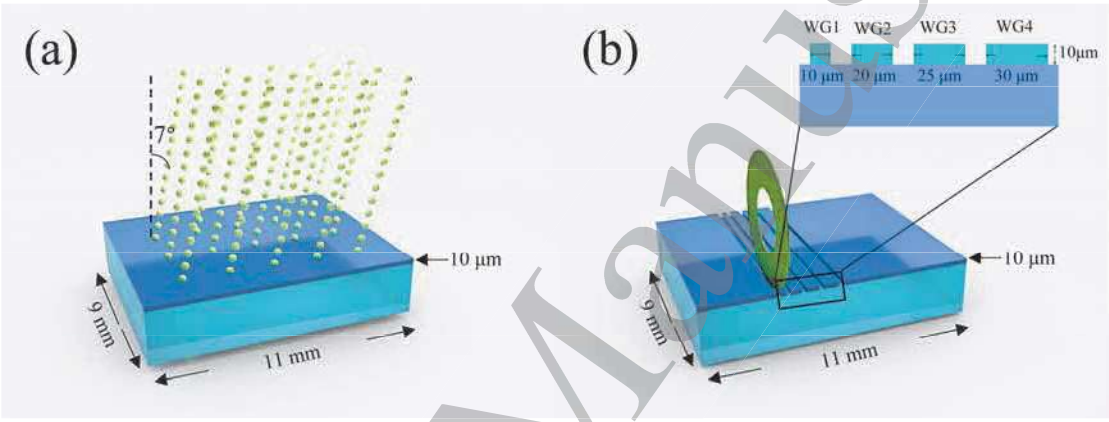

Fig. 1. (color online) Schematic illustrations of (a) 15 MeV C^{5+} ions irradiation and (b) precise diamond blade dicing for Nd:GdCOB ridge waveguides fabrication.

After the fabrication, micro-Raman measurements were carried out to investigate the microstructural modification of Nd:GdCOB crystal using a spectrometer (Horiba/Jobin Yvon HR800). With a detected range of 50-1500 cm^{-1}, the laser beam at 473 nm was focused on the waveguide cross sections and bulk at room temperature.

The μ-SH spectroscopic analysis of the sample was performed to evaluate the nonlinear properties of the waveguides through a confocal microscopy testing platform. The laser beam (with a pulse duration of ~20 ns, a pulse energy of ~2 μJ, and a pulse repetition rate of ~5 MHz) at 1030 nm produced by a microjoule ultrafast fiber laser system (ANTAUS- 10W-2u/5M) was coupled into the sample with a 100× objective (N.A. = 0.3). The reflected μ-SH signal was collected by the same objective, and after passing through several mirrors and lenses, the signal was detected by a spectrometer.

Accepted Manuscript

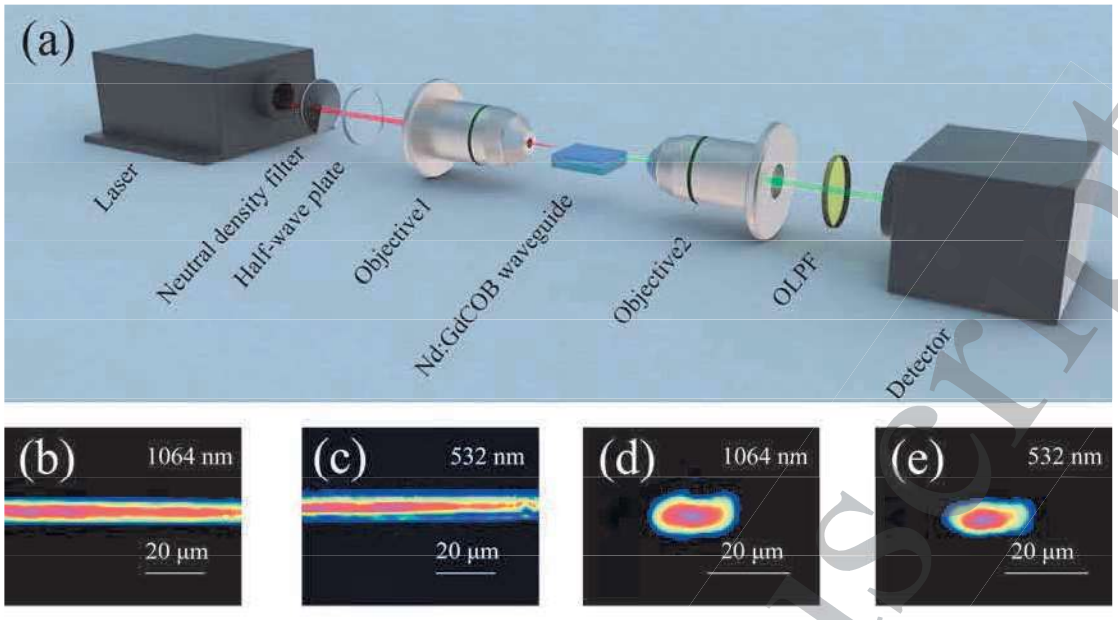

Fig. 2 (color online) (a) The end-face coupling arrangement for SHG characterizations of Nd:GdCOB waveguides. The mode field distribution of planar and WG3 ridge waveguide at 1064 nm ((b) and (d)) and at 532 nm ((c) and (e)).

As shown in Fig. 2 (a), we performed SHG characterization experiments based on an end-face coupling equipment. After the 1064-nm light beam was emitted from the pulsed laser (with a pulse width of ~11.05 ns, a pulse energy of ~80 μJ, and a repetition rate of ~5 kHz), its power and polarization were adjusted by a neutral density filter and a half-wave plate, respectively. A microscope objective (25×, N.A. = 0.4) was used for optical in-coupling. The SHG and residual fundamental signals output from the waveguides were collected by another microscope objective. In order to detect the SHG signal, we used a spectrometer and a powermeter behind an optical low-pass filter (OLPF), which has a transmittance of ~98% at 532 nm and a reflectivity of >99% at 1064 nm. Fig. 2b-e present the fundamental modes along TM and SH modes along TE in planar and WG3 ridge waveguides (all the ridge waveguides show similar modal distributions), respectively. Both fundamental and SH waves are well-confined in the waveguiding regions, showing nearly single-mode profiles, which are very beneficial for SHG.

3. Results and discussion

Accepted Manuscript

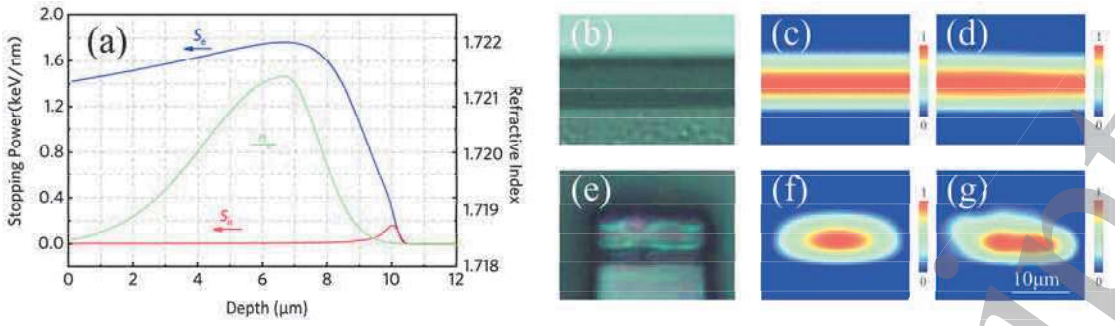

Fig. 3. (color online) (a) The curves of the electronic stopping power (blue line) and the nuclear stopping power (red line) distribution, as well as the refractive index profile of the waveguide (green line), as functions of the depth. Figures (b) and (e) show the microscopic images of the cross sections of planar and WG2 ridge waveguides, respectively. Experimental ((c) and (f)) and simulation ((d) and (g)) results of the modal profiles of planar and WG2 ridge waveguide along TE at 1064 nm, respectively.

The nuclear (S_n) and electronic (S_e) stopping power profiles of 15 MeV C^{5+} ions in Nd:GdOCB were calculated using the SRIM-2008 (Stopping and Range of Ions in Matter 2008) code, and the results are shown in Fig. 3(a). The non-zero S_e is observed within the ion penetration range of 0-10 μm, peaking at approximately 1.7 keV/nm with a depth value of ~6.7 μm. In contrast, the S_n value remains zero within the first 9-μm depth and reaches a maximum of 0.16 keV/nm around 10 μm beneath the surface. Therefore, the electronic damage is considered to be the main cause for the refractive index change at the ion-irradiated area, whereas the nuclear damage at the end of the ion trajectory is responsible for the optical barrier creation. Moreover, the formation of the waveguide layer is a collective effect of both S_n and S_e. The maximum modification of refractive index in the waveguide region is about 0.003 estimated by formula (1):

$$\Delta n = \frac{\sin^2 \Theta_m}{2n} \quad (1)$$

where Θ_m is the maximum incident angle at which the laser beam cannot be focused into the waveguide by the microscope objective, and n=1.7184 is the refractive index of the Nd:GdCOB crystal [32]. Therefore, taking the stopping power profiles as references, we reconstructed the refractive index distribution (see Fig. 3 (a)). Fig. 3 (b) and (e) demonstrate the microscopic images of the planar waveguide and the WG2 ridge waveguide, respectively. The thickness of the modified layer is observed to be

Accepted Manuscript

around 10 μm, which is in fairly good agreement with the calculation performed using the SRIM-2008 code [38]. We imported the index profile into the Rsoft Beam PROP 8.0 [39], and simulated the near-field modal distribution. Taking planar waveguide and WG2 ridge waveguide for example, Fig. 3 (c) and (f) display the simulated near-field distributions at 1064 nm, which are very similar to the experimental results imaged by a CCD camera in the end-face coupling setup (see Fig. 3(d) and (g)), suggesting the reasonability of the reconstructed refractive index profile.

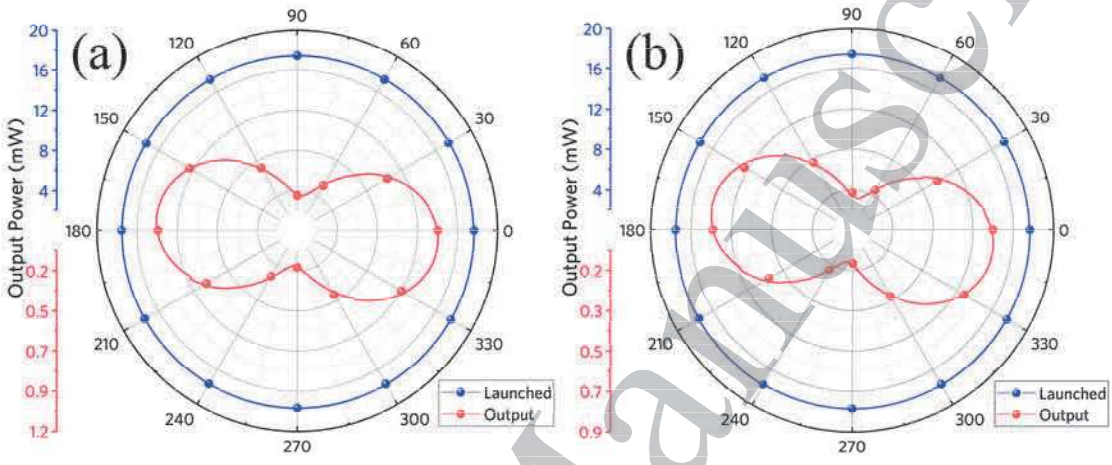

Fig. 4. Output power of (a) planar and (b) WG3 ridge waveguide as a function of all-angle 1064 nm laser transmission with a constant launched power of 17.4 mW under continuous wave (cw) configuration.

To investigate the polarization-dependent properties of the waveguides, the all-angle optical transmission of the fabricated waveguide at 1064 nm has been measured. As one can see from Fig. , for both planar and WG3 ridge waveguides (all the ridge waveguides show similar results), the output power reaches its maxima (0.86 mW and 0.62 mW) along TE polarization (0° and 180°), while decreasing to its minima (0.22 mW and 0.16 mW) along TM polarization (90° and 270°). However, the SHG process occurs under $TM^{\omega} \rightarrow TE^{2\omega}$ process in Nd:GdCOB waveguides, so the polarization-dependent effect has a negative impact on the frequency-doubled output power and conversion efficiency of SHG.

Accepted Manuscript

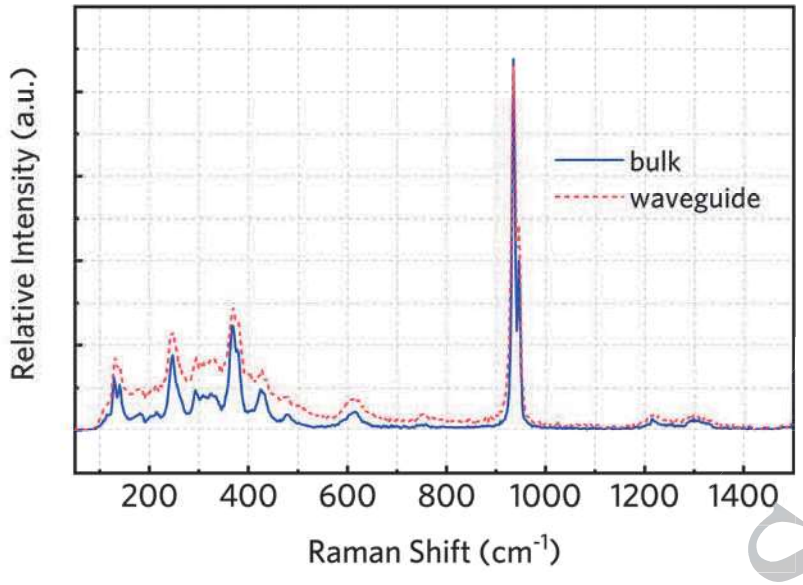

Fig. 5. (color online) Micro-Raman spectra obtained from the WG3 ridge waveguide (red line) and the bulk (blue line) of the Nd:GdCOB crystal.

Micro-Raman spectra of the Nd:GdCOB at substrate and C^{5+} ion implantation region are presented in Fig. . The Raman peak number and position show no differences between the bulk and waveguide areas. However, the Raman intensity in the waveguide increases with respect to the bulk, which may be a result of the lattice expansion attributed to the electronic collisions during the ion irradiation[40-42]. It is also possible that C^{5+} ion implantation has caused more point defects in the crystal, leading to the slight broadening of the Raman peak half-width.

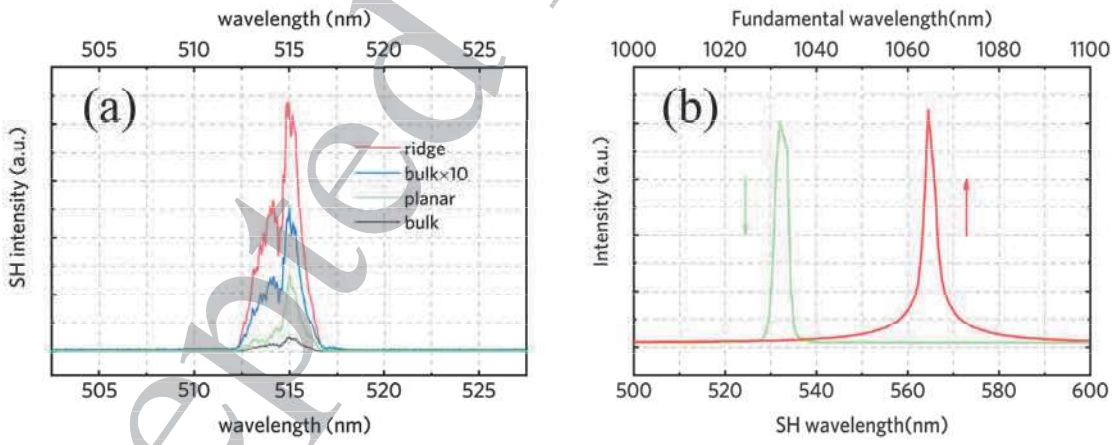

Fig. 6. (color online) (a) The emitted intensity spectra of μ-SH when the laser beam (at 1030 nm) is focused at the WG3 ridge waveguide (red line), the planar waveguide (green line), and the bulk (gray line). (b) The laser spectra of the fundamental beam at 1064 nm (red line) and the second harmonic generation at 532 nm (green line) in WG3 ridge waveguide.

The μ-SH responses of the ridge and planar waveguides, as well as the bulk area, are investigated, as shown in Fig. (a). From the SH intensity profiles, the intensity

Accepted Manuscript

distributions for the bulk, planar, and ridge waveguides have similar shapes, with their peaks at the same position. However, the SH signal in the WG3 ridge waveguide (all the ridge waveguides show similar results) is enhanced significantly, around ten times larger than that in the bulk. It is evident that the nonlinear properties of the Nd:GdCOB crystal are well retained and further greatly enhanced in the waveguide. As showed in Fig. (b), the measured spectra by the pulsed laser pump of the fundamental (at 1064 nm) and SH (at 532 nm) waves from the WG3 ridge waveguide clearly depict the nonlinear process of SHG in Nd:GdCOB waveguides. The 1064-nm fundamental and SH waves are determined to be TM- and TE-polarized, respectively. This verifies that the SHG process occurs under the $TM^{\omega} \rightarrow TE^{2\omega}$ process, which is in good accordance with the phase matching configuration of the bulk.

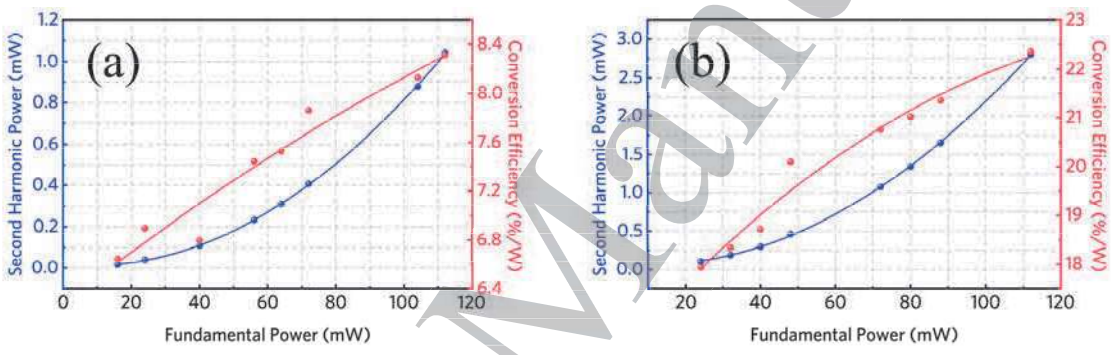

Fig. 4. (color online) Second harmonic power and the corresponding conversion efficiency as functions of the fundamental pump power in (a) planar and (b) WG4 ridge waveguides.

Fig. 4 illustrates the second harmonic powers (in average power) and the conversion efficiencies as functions of the 1064-nm fundamental pump power for planar and WG4 ridge waveguide (WG4 has the best frequency doubling performance of any ridge waveguides) under the pulsed configuration. The measured data points are marked with the solid circles (blue color for the SH powers, and red color for the conversion efficiencies). For the planar waveguide, the maximum average power output of the SH light is ~1.04 mW with a pump power of ~112 mW, resulting in a conversion efficiency of $\eta \approx 8.32\%W^{-1}$. The maximum average output power of the SH light for the WG4 ridge waveguide is ~2.80 mW, which is around twice times larger than that of the planar waveguide. The conversion efficiency reaches a maximum value of $\sim 22.36\%W^{-1}$, leading to a significant enhanced performance. The

Accepted Manuscript

annealing treatment at 260 ℃ for about 30 minutes was carried out in order to observe the changes of related nonlinear properties. However, this thermal operation has negligible influences on the SHG performance of waveguides. The maximum SHG output power (P_{max}), the conversion efficiency (η_{max}), and the propagation losses (α) data for all ridge waveguides are summarized in Table 1, and the related properties of the planar waveguide are also included for references. With an increase in the width of the ridge waveguide, the corresponding maximum SHG power and conversion efficiency will be enhanced. The similar dependence on the ridge width of the SHG properties can also be found in previously reported KTP ridge waveguides [26]. Furthermore, ridge waveguides show better performance in frequency doubling compared to the planar waveguide, mainly due to the more compact structure of the ridge waveguide, which leads to stronger light intensity confined in limited volume. The propagation losses of the ridge waveguides decrease with the increase of ridge widths. And all ridge waveguides have higher propagation losses than the planar waveguide, mainly owing to the relatively high waveguide side-wall roughness caused by the dicing process. By optimizing the dicing parameters, such as the blade type and its rotation velocity, the roughness of the waveguide sidewall can be lowered, thereby reducing the propagation loss of the fabricated ridge waveguide[43]. In addition, the reduction of waveguide side-wall roughness can be also realized by using ion beam milling[44]. Frequency doubling efficiency will be improved if waveguide losses are optimized and self-frequency-doubling effect can be expected.

Accepted Manuscript

Table 1.The maximum output SH powers (P_{max}) and the corresponding conversion efficiencies (η_{max}) and propagation losses (α) of the Nd:GdCOB planar and ridge waveguides.

	WG1	WG2	WG3	WG4	Planar
Width (μm)	10	20	25	30	-
P_{max} (mW)	2.41	2.53	2.68	2.80	1.04
η_{max}(%W^{-1})	19.22	20.23	21.35	22.36	8.32
α (dB/cm)	8.5	7.5	7.2	6.9	5.7

4. Conclusions

We have fabricated ridge waveguides in Nd:GdCOB crystals through the combination of carbon ion irradiation and precise diamond blade dicing. Based on an end-face coupling setup, the optical waveguiding properties of both Nd:GdCOB ridge waveguides and planar waveguide are experimentally investigated. The simulated modal profiles agree well with the measurements, suggesting the rationality of the constructed index profile based on stopping powers. From the micro-Raman spectrum, lattice expansion occurs during the carbon ion implantation with more point defects. The nonlinear properties of the Nd:GdCOB crystal have been fully preserved and greatly enhanced within the waveguides through μ-SH analysis. The SHG at 532 nm based on Type I phase matching has been observed under 1064-nm pulsed laser configuration. The maximum SH power is ~2.80 mW obtained in WG4 ridge waveguide, and the corresponding conversion efficiencies is ~22.36%W^{-1}. For planar waveguides, the maximum SH power is ~1.04 mW with a conversion efficiency of 8.32%W^{-1}. Our work demonstrates that carbon ion irradiation combined with precise diamond blade dicing can be used to fabricate efficient nonlinear waveguides, providing potential applications in integrated photonics.

Acknowledgements

The authors also thank Dr. Y. Cheng for waveguide fabrication and Prof. H. Yu for μ-SH analysis.

Accepted Manuscript

Reference

1. Jia Y C, Chen F, Aldana J R V d, Akhmadaliev S and Zhou S Q 2012 *Opt. Mater.* **34** 1913
2. Murphy E J 1999 *Integrated Optical Circuits and Components: Design and Applications* (New York: Marcel Dekker)
3. Kip D 1998 *Appl. Phys. B: Lasers Opt.* **67** 131
4. Stegeman G I and Seaton C T 1985 *J. Appl. Phys.* **58** R57
5. Grivas C 2011 *Prog. Quantum Electron.* **35** 159
6. Liu Y A, Yan X S, Wu J W, Zhu B, Chen Y P and Chen X F 2020 *Sci. China: Phys., Mech. Astron.* **64** 234262
7. Jia Y C, Wang S X and Chen F 2020 *Opto-Electron. Adv.* **3** 190042
8. Chen F 2008 *Crit. Rev. Solid State Mater. Sci.* **33** 165
9. Jia Y C, Wang L and Chen F 2021 *Appl. Phys. Rev.* **8** 011307
10. Chen F 2012 *Laser Photonics Rev.* **6** 622
11. Jia Y C and Chen F 2019 *Chin. Opt. Lett.* **17** 012302
12. Chen F, Amekura H and Jia Y C 2020 *Ion Irradiation of Dielectrics for Photonic Applications* (Singapore: Springer Nature) p.6
13. Wesch W and Wendler E 2016 *Ion Beam Modification of Solids* (Cham: Springer Nature) p.153
14. Li Z Q and Chen F 2017 *Appl. Phys. Rev.* **4** 011103
15. Townsend P D, Chandler P J and Zhang L 1994 *Optical Effects of Ion Implantation* (Cambridge: Cambridge University Press)
16. Chen F, Wang X L and Wang K M 2007 *Opt. Mater.* **29** 1523
17. Chen F 2009 *J. Appl. Phys.* **106** 081101
18. Bentini G G, Bianconi M, Chiarini M, Correra L, Sada C, Mazzoldi P, Argiolas N, Bazzan M and Guzzi R 2004 *J. Appl. Phys.* **92** 6477
19. Jia Y C, Rüter C E, Akhmadaliev S, Zhou S, Chen F and Kip D 2013 *Opt. Mater. Express* **3** 433
20. Jia Y C, Tan Y, Cheng C, Aldana J R V d and Chen F 2014 *Opt. Express* **22** 12900
21. Jia Y C, Dong N N, Chen F, Aldana J R V d, Akhmadaliev S and Zhou S Q 2012 *Opt. Mater. Express* **2** 657
22. Siebenmorgen J, Petermann K, Huber G, Rademaker K, Nolte S and Tünnermann A 2009 *Appl. Phys. B: Lasers Opt.* **97** 251
23. Okhrimchuk A G and Shestakov A V 2005 *Opt. Lett.* **30** 2248
24. Chen F and Aldana J R V a d 2014 *Laser Photonics Rev.* **8** 251
25. Cheng Y Z, Liu J M, Akhmadaliev S, Zhou S Q, Kong Y F and Chen F 2015 *Opt. Mater.* **48** 209
26. Chen C, Ruter C E, Volk M F, Chen C, Shang Z, Lu Q M, Akhmadaliev S, Zhou S Q, Chen F and Kip D 2016 *Opt. Express* **24** 16434
27. Lu J H, Li G M, Liu J H, Zhang S J, Chen H C, Jiang M H and Shao Z S 1999 *Opt. Commun.* **168** 405
28. Wang C Q, Chow Y T, Gambling W A, Zhang S J, Shao Z S and Chen H C 2000

Accepted Manuscript

Opt. Commun. **174** 471
29. Mougel F, Aka G, Kahn-Harari A, Hubert H, Benitez J M and Vivien D 1997 *Opt. Mater.* **8** 161
30. Aka G, Mougel F, Auge F, Kahn-Harari A, Vivien D, Benitez J M, Salin F, Pelen D, Balembois F, Georges P, Brun A, Nain N L and Jacquet M 2000 *J. Alloys Compd* **303** 401
31. Du J H, Wang J Y, Yu H H and Zhang H J 2019 *Opt. Lett.* **45** 327
32. Ren Y Y, Jia Y C, Chen F, Lu Q M, Akhmadaliev S and Zhou S Q 2011 *Opt. Express* **19** 12490
33. Jia Y C, Aldana J R V a d, Lu Q M, Jaque D and Chen F 2013 *J. Lightwave Technol.* **31** 3873
34. *Disco Co., < http://www.disco.co.jp>*
35. Zhang J, Chen J Y, Yan L, Wang Y S, Zhang L L, Yue Q Y, Zheng Y L and Liu C X 2021 Vacuum **193** 1104932
36. Zhou Y F, Wang L, Liu P, Liu T, Zhang L, Huang D T and Wang X L 2014 Nucl. Instrum. Methods Phys. Res., Sect. B **326** 110
37. Zhao J H, Jiao X S, Ren Y Y, Gu J J, Wang S M, Bu M L and Wang L 2021 Chin. Opt. Lett. **19** 060009
38. *J. F. Ziegler, Computer code, SRIM, 2012, <http://www.srim.org>*
39. *RSoft Design Group, Computer software: BeamPROP, 2013, <http://www.rsoftdesign.com>*
40. He S, Zhang Z, Liu H, Akhmadaliev S, Zhou S, Wang X and Wu P 2019 *Applied Physics Express* **12** 076502
41. Pandey P, Bitla Y, Zschornak M, Wang M, Xu C, Grenzer J, Meyer D-C, Chin Y-Y, Lin H-J, Chen C-T, Gemming S, Helm M, Chu Y-H and Zhou S 2018 *APL Materials* **6** 066109
42. Chen C, Wang C, Cai X, et al 2019 *Nanoscale* **11** 8110
43. Volk M F, Rüter C E, Santandrea M, Eigner C, Padberg L, Herrmann H, Silberhorn C and Kip D 2018 *Opt. Mater. Express* **8** 82
44. Degl'Innocenti R, Reidt S, Sorianello A, Rezzonico D, Poberaj G and Günter P 2006 J. Appl. Phys. **100** 123121

Accepted Manuscript